Exploring the occurrence of thioflavin-T-positive insulin amyloid aggregation intermediates

Mantas Ziaunys*, Andrius Sakalauskas, Kamile Mikalauskaite, Vytautas Smirnovas

Institute of Biotechnology, Life Sciences Center, Vilnius University, Vilnius, Lithuania

*Corresponding Author:

Mantas Ziaunys

Sauletekio al. 7, Vilnius, LT-10257, Lithuania

Email address: mantas.ziaunys@gmc.vu.lt

Abstract

The aggregation of proteins is considered to be the main cause of several neurodegenerative diseases. Despite much progress in amyloid research, the process of fibrillization is still not fully understood, which is one of the main reasons why there are still very few effective treatments available. When the aggregation of insulin, a model amyloidogenic protein, is tracked using thioflavin-T (ThT), an amyloid specific dye, there is an anomalous occurrence of double-sigmoidal aggregation kinetics. Such an event is likely related to the formation of ThT-positive intermediates, which may affect the outcome of both aggregation kinetic data, as well as final fibril structure. In this work we explore insulin fibrillization under conditions, where both normal and double-sigmoidal kinetics are observed and show that, despite their dye-binding properties and random occurrence, the ThT-positive intermediates do not significantly alter the overall aggregation process.

Introduction

Protein aggregation into amyloid fibrils is linked to multiple neurodegenerative disorders, such as Alzheimer's, Parkinson's or prion diseases (Knowles, Vendruscolo & Dobson, 2014; Chiti & Dobson, 2017), affecting millions of people worldwide (Isik, 2010). Such protein assembly into insoluble aggregates is still not fully understood, despite the significant effort put into figuring

28 out both the mechanism of aggregation (Meisl et al., 2016; Castello et al., 2017; Biza et al.,
29 2017; Giorgetti et al., 2018; Linse, 2019), as well as the resulting fibril structural aspects (Makin
30 & Serpell, 2005; Fitzpatrick et al., 2013). As a consequence, there are still very few disease
31 modifying drugs available (Mehta et al., 2017; Cummings et al., 2019; Maurer et al., 2018; Park
32 et al., 2020).

33 The process of amyloid fibril formation consists of multiple microscopic events. The first one
34 being nucleation, a process during which proteins lose their native structure and form a primary
35 aggregation center (Chatani & Yamamoto, 2018). This structure then passes several growth
36 phases, such as elongation (Gurry & Stultz, 2014), assembly into protofibrils (Dolui et al., 2018)
37 and subsequent maturation into fully formed fibrils (Ma et al., 2013; Sidhu et al., 2017). The
38 resulting aggregates are then capable of acting as catalysts for surface-mediated secondary
39 nucleation (Törnquist et al., 2018), as well as fragmenting into smaller fibrils (Nicoud et al.,
40 2015), thus creating new aggregation centers. Different proteins have also been shown to form
41 specific oligomeric species prior to further aggregation processes (Nettleton et al., 2000; Chiti &
42 Dobson, 2006; Danzer et al., 2007; Selivanova & Galzitskaya, 2012; Sengupta, Nilson & Kayed,
43 2016). Such a large number of possible steps involved in the aggregation process significantly
44 complicates matters and requires extensive research in order to understand and prevent the
45 progress of amyloid-related diseases.

46 In order to study aggregation reactions *in vitro*, insulin is often used as a model amyloidogenic
47 protein (Brange et al., 1997). Despite its main application as a treatment for diabetes, insulin is
48 capable of forming amyloid fibrils under acidic or neutral pH at an elevated temperature (Nielsen
49 et al., 2001). This, coupled with its availability, has made it a widely used protein to study both
50 the mechanisms of amyloid formation (Ahmad et al., 2003; Podestà et al., 2006; Malik & Roy,
51 2011), as well as possible inhibitory compounds (Wang, Dong & Sun, 2012; Malisauskas et al.,
52 2015; Zheng & Lazo, 2018). Even though a large number of experiments have been conducted
53 with insulin under various conditions, new information regarding its fibrillation continues to
54 arise, such as new possible aggregation mechanisms or structural polymorphisms (Sakalauskas,
55 Ziaunys & Smirnovas, 2019; Ratha et al., 2020). A factor that requires further attention is the
56 seemingly random appearance of double-sigmoidal aggregation kinetics when examining the
57 fibrillization of insulin with a fluorescent probe – thioflavin-T (ThT). This phenomenon was
58 examined by Smirnovas *et al.* (Smirnovas & Winter, 2008), Grudzielanek *et al.* (Grudzielanek,
59 Smirnovas & Winter, 2006) and Fodera *et al.* (Foderà et al., 2009), where it was shown that the
60 first increase in the double-sigmoidal curve is likely related to the formation of oligomeric
61 intermediate species capable of binding ThT and this event was consistently reproducible only
62 under certain environmental conditions.

63 ThT is a benzothiazole dye that binds to the beta-sheet grooves of amyloid fibrils and attains a
64 locked conformation (Robbins et al., 2012). This causes a red shift of its excitation and emission
65 wavelengths, as well as a significant increase in fluorescence quantum yield (Gade Malmos et
66 al., 2017; Xue et al., 2017). The fluorescence intensity, binding affinity and maximum

67   excitation/emission wavelengths are highly dependent on the conformation of fibrils and there
68   are even reports of multiple types of binding modes on the same type of aggregate (Sidhu et al.,
69   2018; Ziaunys, Sneideris & Smirnovas, 2020). Despite being widely used as a probe to track
70   amyloid formation, the dye's fluorescence is not exclusively tied to such fibrillar aggregates, as it
71   has been shown to increase in fluorescence upon binding or being trapped in non-amyloid
72   structures (Singh et al., 2010; Sulatskaya et al., 2018). This, in turn, does not rule out the
73   possibility of the double-sigmoidal kinetics being the result of structures that are not amyloid in
74   nature.

75   In our research we observed that when human recombinant insulin is aggregated at pH 2.4, there
76   exist both regular sigmoidal fibrilization kinetic curves, as well as double-sigmoidal ones under
77   the same aggregation conditions. Unlike in the previously reported cases (Grudzielanek,
78   Smirnovas & Winter, 2006; Smirnovas & Winter, 2008; Foderà et al., 2009), this occurrence
79   appears to be random even when the same batch of protein is used. The double-sigmoidal curves
80   also possess a different ThT fluorescence intensity at the end of the reaction, which begs the
81   question whether the formation of these anomalous ThT-positive intermediates could yield
82   differently structured fibrils. Small variations in insulin aggregation conditions, such as pH value
83   or protein concentration (Sneideris et al., 2015; Sakalauskas, Ziaunys & Smirnovas, 2019) can
84   cause the formation of distinct conformation aggregates. Since both regular and double-
85   sigmoidal aggregation types exist under the same conditions, this creates an opportunity to
86   explore any possible differences during the whole fibrillization process. In this work we examine
87   a large sample size of insulin aggregation kinetic curves, isolate the double-sigmoidal kinetic
88   samples from regular ones and determine whether there are secondary structure, morphology,
89   ThT binding and seeding propensity differences between them. In addition, both regular and
90   double-sigmoidal aggregation reactions are tracked by scanning ThT fluorescence excitation-
91   emission matrices in order to determine if there are aggregate structural differences from distinct
92   dye binding, such as specific maximum excitation and emission wavelengths or bound-ThT
93   fluorescence intensity (Groenning et al., 2007; Ziaunys & Smirnovas, 2019b; Ziaunys,
94   Sakalauskas & Smirnovas, 2020).

Materials and Methods

Insulin aggregation

97   Human recombinant insulin powder (Sigma-Aldrich cat. No. 91077C) was dissolved in a 100
98   mM sodium phosphate buffer (pH 2.4) containing 100 mM NaCl (reaction buffer). ThT (Sigma-
99   Aldrich cat. No. T3516) was dissolved in H_2O to a final concentration of ~12 mM and mixed for
100   10 min using vigorous agitation, after which the dye solution was filtered through a 0.22 μm
101   pore syringe filter. An aliquot of the ThT stock solution was diluted 200 times and the exact dye
102   concentration was determined by measuring the solution's absorbance at 412 nm ($\varepsilon_{412} = 23\ 250$
103   $M^{-1}cm^{-1}$). The ThT stock solution was then diluted to a final concentration of 10 mM. The
104   protein solution was then combined with the reaction buffer and a 10 mM ThTsolution to a final

105   protein and ThT concentration of 100 µM (insulin ε_{280}=6335 M^{-1}cm^{-1}, MW=5808 Da) and
106   distributed into 200 µL test tubes (20 µL final volume). These conditions result in both types of
107   aggregation, with a random appearance of double-sigmoidal kinetic curves.

108   The aggregation kinetics were tracked as previously described (Milto, Michailova & Smirnovas,
109   2014). In short, sample ThT fluorescence intensity was monitored using a Qiagen Rotorgene Q
110   real-time analyzer at a constant 60°C temperature with measurements taken every minute. A total
111   of one thousand samples were measured in batches of 36. After the aggregation reaction, the
112   samples were stored at 4°C.

113   For seeded aggregation, fibril samples were sonicated for 10 min using a Bandelin Sonopuls
114   ultrasonic homogenizer with a MS73 tip (40% power, with 30 s sonication / 30 s rest intervals).
115   Then insulin, ThT and fibril solutions were combined to a final protein concentration of 100 µM,
116   ThT concentration of 100 µM and 1% or 10^{-5}% fibrils (% of total protein mass in solution). The
117   reaction was monitored as in the non-seeded aggregation experiment.

118   **Kinetic data analysis**

119   A first-order derivative was calculated for each sample's kinetic data, using a 40-point averaging
120   range. The maximum value of the derivative curve corresponds to the rate of aggregation, while
121   its position – to the time at which the rate is highest (t_r). Samples which had one clear peak in the
122   first-order derivative were regarded as normal, while ones which were composed of two peaks
123   (regular, high-rate peak and a small, low-rate peak preceding it) - as double-sigmoidal. Data
124   processing was done using Origin 2018 software.

125   **Fluorescence measurements**

126   Each sample was diluted 5 times to 100 µL with the reaction buffer containing 100 µM of ThT
127   and their fluorescence intensity was measured using a Varian Cary Eclipse Fluorescence
128   Spectrophotometer with 440 nm excitation (slit width – 5 nm) and 480 nm emission (slit width –
129   5 nm) wavelengths. For each case, three measurements were taken and averaged.

130   **Atomic force microscopy**

131   The samples were separated into two groups based on their aggregation kinetic profiles and
132   mixed to result in a homogenous solution. 30 µL aliquots were deposited on freshly cleaved
133   mica, incubated for 1 min, washed with 1 mL of MilliQ water and dried under airflow. In the
134   case of intermediate aggregates during the double-sigmoidal aggregation, the real-time analyzer
135   was stopped when the aggregation curve reached the first minor plateau. Then the samples were
136   quickly removed and placed on freshly cleaved mica as mentioned earlier. For each condition,
137   three 10 x 10 µm AFM images were recorded as previously described (Sneideris et al., 2019)
138   using a Dimension Icon (Bruker) atomic force microscope, operating in tapping mode with a
139   silicon cantilever Tap300AI-G (40 N m^{-1}, Budget Sensors). High resolution (1024 x 1024 pixels)
140   images were flattened and analyzed using Gwyddion 2.5.5 and SPIP 6.7.8. Each fibril's height

141   was determined by tracing lines perpendicular to the fibril's axis. Height statistical analysis was
142   conducted by taking into consideration all three repeats for each condition, i.e. a similar number
143   of aggregates were examined in every image.

Fourier-transform infrared spectroscopy

145   The two sample groups were centrifuged at 10'000 g for 30 min and resuspended in 1 mL of
146   D_2O. The centrifugation and resuspension step was repeated 3 times and the final resuspension
147   volume was 0.25 mL. Before measurements, both samples were sonicated using a Bandelin
148   Sonopuls ultrasonic homogenizer with a MS72 tip (20% power and constant sonication for 30 s).
149   Sonication helps to break fibril clumps, which leads to less scattering effects and better-quality
150   FTIR spectra. During sample preparation and measurement, H-D exchange is insignificant, as in
151   the case of insulin fibrils it is very slow (Dzwolak, Loksztejn & Smirnovas, 2006). The spectra
152   were recorded as previously described (Sneideris et al., 2019). In short, the concentrated fibril
153   samples were scanned in near-vacuum conditions (~2 mbar) at room temperature using a Vertex
154   80v (Bruker) IR spectrometer. 256 interferograms were averaged for each spectrum. A D_2O
155   spectrum was subtracted and the resulting spectra were normalized to the same area of amide I/I'
156   band (1700-1595 cm^{-1}). Data processing was performed using GRAMS software.

ThT fluorescence excitation-emission matrices

158   The aggregation solution was prepared as described in the insulin aggregation section to a final
159   volume of 3 mL. The solution was then placed in a 10 mm pathlength cuvette, sealed with a plug
160   cap to prevent evaporation and incubated at 60°C without agitation. EEMs were scanned every 5
161   min using a Varian Cary Eclipse fluorescence spectrophotometer using an excitation range from
162   440 to 465 nm and emission range from 475 to 500 nm (excitation and emission slit widths – 5
163   nm, wavelength step – 1 nm, scan rate – 600 points/min). Due to the analysis being conducted on
164   a transitioning system, the EEM size was optimized to be as minimal as possible to lower the
165   impact of an intensity drift, which results from different concentrations of aggregates present at
166   the start and finish of each scan cycle. This was done by first acquiring a larger EEM, which
167   encompassed the maximum ThT fluorescence zone, then it was narrowed down as much as
168   possible to reduce scan time.

169   Each EEM was corrected for the inner filter effect caused by 100 µM of ThT as described
170   previously (Ziaunys & Smirnovas, 2019b). In short, the correction was made by using the
171   absorbance spectra of 100 µM non-bound ThT, as it is extremely difficult to account for
172   absorbance changes throughout the entire reaction resulting from ThT becoming bound to fibrils
173   and because the majority of ThT remains non-bound even when all insulin is aggregated
174   (Ziaunys & Smirnovas, 2019b). The EEM "center of mass" was then calculated for the entire
175   EEM after the inner filter correction. This was done to prevent signal noise, caused by light
176   scattering, from affecting the maximum intensity position.

177

178

Results

Aggregation kinetics

181 A large number (n=1 000) of low volume insulin samples were aggregated under the exact same
182 conditions and their kinetics were tracked by monitoring changes in ThT fluorescence intensity.
183 Analysis of all the data revealed that a majority of samples experienced normal, sigmoidal
184 spontaneous aggregation kinetics, with one rate maximum seen in the first order derivative
185 (Figure 1A, C). A fraction of samples displayed double-sigmoidal kinetics, with two peaks in the
186 first order derivative curve (Figure 1B, D). The first increase in fluorescence intensity of the
187 double-sigmoidal aggregation kinetics occurred roughly 100 minutes before the second increase
188 and its rate was, on average, nearly 10-fold lower.

189 A total of 55 samples possessed such unusual aggregation kinetics, constituting a probability of
190 such an occurrence being at least 5.5 % under the tested conditions. 77 samples had an
191 intermediate kinetic profile (very small first peak or a large overlap between both peaks), which
192 could not be accurately attributed to either type of aggregation. The normal and double-
193 sigmoidal samples were then separated for further analysis.

194 In order to determine if there are any links between the rate of aggregation, the time at which this
195 rate is highest and the resulting fluorescence intensity of fibrils, all three factor dependencies
196 were examined. We can see that all three parameters are mostly independent from one another
197 (Figure 2A-C). The time at which the aggregation rate is highest, does not influence the rate at
198 which fibril elongation occurs, neither does it change the final fluorescence intensity of the
199 formed fibrils. When we compare these three factors between the normal and double-sigmoidal
200 samples (Figure 2D-I)), it appears that the double-sigmoidal fibrillization has a slightly lower
201 time at which the maximum aggregation rate is reached (Figure 2D, G) and it has no effect on
202 the rate itself (Figure 2E, H). There is, however, a considerable difference in the final
203 fluorescence intensity distribution (Figure 2F, I). The distribution maximum is more than 10%
204 lower when the aggregation kinetics are double-sigmoidal, suggesting that there are either off-
205 pathway aggregates or a fraction of fibrils possess a different ThT binding mode. Despite this
206 distinction in average fluorescence intensity, a large portion of all three data sets overlap with
207 one another due to a large spread caused by the stochastic nature of non-seeded insulin
208 aggregation (Foderà et al., 2008).

Fibril structure and seeding properties

210 The fibril samples were examined using atomic force microscopy (AFM), Fourier-transform
211 infrared spectroscopy (FTIR) and used as seeds to examine their rate of self-replication. In the

212   AFM images acquired during the first increase in signal intensity during double-sigmoidal
213   kinetics, we observe small, round oligomeric aggregate species (with most having a height of 1
214   to 2 nm) and short protofibrils (0.1 to 0.5 μm in length) (Figure 3A, Figure S1). When compared
215   to a sample obtained before an increase in dye fluorescence is observed (Figure S1), there are far
216   more aggregates present in the case of ThT-positive intermediates. The ThT-negative samples
217   also contain a higher number of 0.5 – 1.5 nm height assemblies and very few elongated
218   structures (Figure S2A-C). When the aggregation reactions are concluded, the fibrils are
219   considerably longer and have a greater height, however, there do not seem to be any major
220   differences between both cases, neither visually nor by their height distribution (Figure 3B-D,
221   Figure S1). Due to formation of large aggregate clumps, the fibrils were sonicated to better
222   examine any possible differences in their height. While the height distribution average values are
223   similar, there is a wider spread in the case of the sonicated double-sigmoidal sample (Figure S3),
224   likely caused by the existence of several smaller fibrils or amorphous aggregates. The FTIR
225   second derivative spectra (Figure 3E) and seeding kinetics (Figure 3F) are also nearly identical
226   for both cases, indicating that the double-sigmoidal aggregation does not have a significant
227   influence on the final fibril secondary structure or self-replication properties.

228   **ThT-positive intermediates**

229   The normal and double-sigmoidal aggregation reactions were examined by scanning excitation-
230   emission matrices of ThT fluorescence during aggregation. The kinetic curves were plotted as
231   the maximum EEM signal intensity over time. When examining the kinetics of double-sigmoidal
232   aggregation, we see that the lag phase is followed by a slow increase in ThT fluorescence
233   intensity, then a sudden jump in intensity (marked as *), which then quickly returns to a low
234   value and is continued by the second growth phase (Figure 4A). Such a jump is not visible in the
235   normal aggregation data (Figure 4A), nor in any of the previous experiments, where samples
236   were only scanned once a minute. This indicates that it may only be visible for a very short time
237   during the EEM scan. When the excitation and emission wavelengths of the EEM "center of
238   mass" are calculated (Figure 4B, C), we see that there are significant changes in both of these
239   parameters during the first, anomalous increase in ThT intensity, as compared to relatively minor
240   variations in the normal aggregation. The excitation wavelength shifts from 457 nm to 453 nm
241   and then rises back to 454 nm, while the emission intensity shifts between 489 nm and 487 nm
242   and gradually reaches 488 nm. Both wavelengths reach a constant value at roughly the same time
243   after the sudden increase in ThT fluorescence intensity, marking the end of the anomalous phase.

244   If we examine the top fluorescence intensity value distributions in the EEMs before and after the
245   sudden signal jump (Figure 4D), there are both significant shifts in the top value positions during
246   the anomalous phase, as well as single, high intensity lines. Such lines can be caused by either a
247   large particle floating past the optical path during a scan or by sudden association and
248   dissociation of a ThT-positive aggregate. After the high intensity jump, once the signal returns to

249 normal, these lines are no longer present in any of the EEMs (as seen after 290 minutes (Figure
250 4D)) and they become nearly identical. Such an occurrence has been observed multiple times
251 throughout the study and it ranged from being mild (Figure S4) to very extreme (Figure S5).

252 **Discussion**

253 The large sample size of aggregation reactions shows that under these conditions, the occurrence
254 of such anomalous, double-sigmoidal fibrilization kinetics is both relatively rare (5.5%) and
255 seemingly random. This is unlike the previously reported cases, where a certain set of conditions
256 caused all of the kinetic curves to be double-sigmoidal (Grudzielanek, Smirnovas & Winter,
257 2006; Smirnovas & Winter, 2008; Foderà et al., 2009). The conditions used in this work allowed
258 to examine how such peculiar kinetics affected the overall aggregation reaction, as both types of
259 fibrillizations were observed. When compared to normal aggregation, this anomalous event
260 occurs roughly 100 minutes before the second increase, however it does not influence the time at
261 which maximum aggregation rate is reached nor the rate of aggregation and the resulting fibrils
262 have an identical morphology, secondary structure and seeding properties. It is possible that it
263 generates a small population of small, amorphous structures, as hinted by the fibril height range,
264 AFM images and the lower ThT fluorescence intensity distribution. The fact that this anomaly
265 does not influence the overall kinetic parameters (apart from lag time) or fibril structure is a
266 positive aspect, considering that these values are often used to determine the effectiveness of
267 anti-amyloid compounds. However, the random formation of different intermediate species does
268 raise concerns. If these structures can appear in any reaction solution and there is minimal
269 connection between their existence and the overall aggregation process, then there is essentially
270 no way of controlling this event.

271 Judging from the ThT fluorescence EEMs, it appears that during the anomalous aggregation
272 phase, there exists the formation of ThT-positive intermediates or structures that are capable of
273 trapping and conformationally "locking" the dye molecules, unlike during a normal fibrilization
274 process. AFM images acquired during this phase show small and round aggregates, as well as
275 short protofibril species, with an average height that is much lower than observed for fully
276 formed fibrils. Their ability to bind ThT in a different mode (as identified by the higher
277 excitation and emission wavelengths) suggests that they possess a structure that is distinct from
278 both normal intermediate species, as well as the fully formed fibrils. The differences in these
279 parameters could also be an indicator that there is no actual surface-dye interaction, but rather an
280 entrapment of ThT in the oligomeric structure. The lower ThT fluorescence intensity distribution
281 at the end of the reaction and AFM images also hint at a possibility that some of these structures
282 remain in solution and do not become incorporated into the amyloid structure of normal fibrils.

283 A possible explanation for the ThT-binding ability of these intermediates may stem from the
284 high intensity lines seen in the ThT fluorescence EEMs. When the sample is continuously
285 scanned to generate an EEM, such lines can only result from either a larger particle floating past

286 the optical path or by a quick association and dissociation of a ThT positive aggregate.
287 Considering that during fibrilization the concentration of large aggregates increases, an event
288 which results in enhanced light scattering and signal noise, we would expect to observe an
289 increasing amount of such high intensity lines, however, this is not the case. Once the first phase
290 of the double-sigmoidal kinetics is concluded, they are no longer seen, which means that they are
291 likely not the result of light scattering from larger aggregate particles. This leaves the hypothesis
292 that ThT-positive intermediates quickly associate and dissociate during this time period. If these
293 intermediates are capable of trapping ThT molecules within their structure, they may not even
294 require a similarity to amyloids, as it has been shown that ThT immobilization can cause an
295 increase in fluorescence intensity (Hutter et al., 2011; Ziaunys & Smirnovas, 2019a). This would
296 also explain the significantly different excitation and emission wavelengths, as these parameters
297 depend highly on the dye's binding mode.

298 While these ThT-positive intermediates do not have any major effect on the final fibril structure
299 and most kinetic parameters, they could become an issue when testing potential anti-amyloid
300 compounds. If an inhibitor targets the process of primary nucleation and is specific towards a
301 certain type of intermediate structure, the formation of a different type of aggregate, which
302 incorporates ThT but is not amyloid-like, may not be affected at all and result in an increase in
303 ThT fluorescence intensity. This would then lead to a false interpretation on the effectiveness of
304 the tested compound and negatively affect the drug screening process.

305

Conclusions

307 The occurrence of double-sigmoidal kinetics during insulin amyloid aggregation does not
308 influence the final fibril structure or morphology, nor does it change the rate of the main
309 reaction. However, it does result in a lower ThT fluorescence intensity and may be related to the
310 formation of a different type of aggregates. The random variability observed during intermediate
311 oligomer formation may also have a negative impact during potential anti-amyloid drug
312 screenings and lead to false interpretations.

313 **References**

314 Ahmad A, Millett IS, Doniach S, Uversky VN, Fink AL. 2003. Partially Folded Intermediates in
315   Insulin Fibrillation. *Biochemistry* 42:11404–11416. DOI: 10.1021/bi034868o.

316 Biza K V., Nastou KC, Tsiolaki PL, Mastrokalou C V., Hamodrakas SJ, Iconomidou VA. 2017.
317   The amyloid interactome: Exploring protein aggregation. *PLOS ONE* 12:e0173163. DOI:
318   10.1371/journal.pone.0173163.

319 Brange J, Andersen L, Laursen ED, Meyn G, Rasmussen E. 1997. Toward Understanding Insulin
320   Fibrillation. *Journal of Pharmaceutical Sciences* 86:517–525. DOI: 10.1021/js960297s.

321 Castello F, Paredes JM, Ruedas-Rama MJ, Martin M, Roldan M, Casares S, Orte A. 2017. Two-
322   Step Amyloid Aggregation: Sequential Lag Phase Intermediates. *Scientific Reports* 7:40065.
323   DOI: 10.1038/srep40065.

324 Chatani E, Yamamoto N. 2018. Recent progress on understanding the mechanisms of amyloid
325   nucleation. *Biophysical Reviews* 10:527–534. DOI: 10.1007/s12551-017-0353-8.

326 Chiti F, Dobson CM. 2006. Protein Misfolding, Functional Amyloid, and Human Disease. *Annual*
327   *Review of Biochemistry* 75:333–366. DOI: 10.1146/annurev.biochem.75.101304.123901.

328 Chiti F, Dobson CM. 2017. Protein Misfolding, Amyloid Formation, and Human Disease: A
329   Summary of Progress Over the Last Decade. *Annual Review of Biochemistry* 86:27–68. DOI:
330   10.1146/annurev-biochem- 061516-045115.

331 Cummings J, Lee G, Ritter A, Sabbagh M, Zhong K. 2019. Alzheimer's disease drug development
332   pipeline: 2019. *Alzheimer's & Dementia: Translational Research & Clinical Interventions*
333   5:272–293. DOI: 10.1016/j.trci.2019.05.008.

334 Danzer KM, Haasen D, Karow AR, Moussaud S, Habeck M, Giese A, Kretzschmar H, Hengerer
335   B, Kostka M. 2007. Different Species of α-Synuclein Oligomers Induce Calcium Influx and
336   Seeding. *Journal of Neuroscience* 27:9220–9232. DOI: 10.1523/JNEUROSCI.2617-
337   07.2007.

338 Dolui S, Roy A, Pal U, Saha A, Maiti NC. 2018. Structural Insight of Amyloidogenic Intermediates
339   of Human Insulin. *ACS Omega* 3:2452–2462. DOI: 10.1021/acsomega.7b01776.

340 Dzwolak W, Loksztejn A, Smirnovas V. 2006. New Insights into the Self-Assembly of Insulin
341   Amyloid Fibrils: An H−D Exchange FT-IR Study. *Biochemistry* 45:8143–8151. DOI:
342   10.1021/bi060341a.

343 Fitzpatrick AWP, Debelouchina GT, Bayro MJ, Clare DK, Caporini MA, Bajaj VS, Jaroniec CP,
344   Wang L, Ladizhansky V, Muller SA, MacPhee CE, Waudby CA, Mott HR, De Simone A,
345   Knowles TPJ, Saibil HR, Vendruscolo M, Orlova E V., Griffin RG, Dobson CM. 2013.
346   Atomic structure and hierarchical assembly of a cross-β amyloid fibril. *Proceedings of the*
347   *National Academy of Sciences* 110:5468–5473. DOI: 10.1073/pnas.1219476110.

348 Foderà V, Cataldo S, Librizzi F, Pignataro B, Spiccia P, Leone M. 2009. Self-Organization

349   Pathways and Spatial Heterogeneity in Insulin Amyloid Fibril Formation. *The Journal of*
350   *Physical Chemistry B* 113:10830–10837. DOI: 10.1021/jp810972y.

351   Foderà V, Librizzi F, Groenning M, Van De Weert M, Leone M. 2008. Secondary nucleation and
352   accessible surface in insulin amyloid fibril formation. *Journal of Physical Chemistry B*
353   112:3853–3858. DOI: 10.1021/jp710131u.

354   Gade Malmos K, Blancas-Mejia LM, Weber B, Buchner J, Ramirez-Alvarado M, Naiki H, Otzen
355   D. 2017. ThT 101: a primer on the use of thioflavin T to investigate amyloid formation.
356   *Amyloid* 24:1–16. DOI: 10.1080/13506129.2017.1304905.

357   Giorgetti S, Greco C, Tortora P, Aprile F. 2018. Targeting Amyloid Aggregation: An Overview
358   of Strategies and Mechanisms. *International Journal of Molecular Sciences* 19:2677. DOI:
359   10.3390/ijms19092677.

360   Groenning M, Norrman M, Flink JM, van de Weert M, Bukrinsky JT, Schluckebier G, Frokjaer S.
361   2007. Binding mode of Thioflavin T in insulin amyloid fibrils. *Journal of Structural Biology*
362   159:483–497. DOI: 10.1016/j.jsb.2007.06.004.

363   Grudzielanek S, Smirnovas V, Winter R. 2006. Solvation-assisted Pressure Tuning of Insulin
364   Fibrillation: From Novel Aggregation Pathways to Biotechnological Applications. *Journal of*
365   *Molecular Biology* 356:497–509. DOI: 10.1016/j.jmb.2005.11.075.

366   Gurry T, Stultz CM. 2014. Mechanism of Amyloid-β Fibril Elongation. *Biochemistry* 53:6981–
367   6991. DOI: 10.1021/bi500695g.

368   Hutter T, Amdursky N, Gepshtein R, Elliott SR, Huppert D. 2011. Study of Thioflavin-T
369   Immobilized in Porous Silicon and the Effect of Different Organic Vapors on the
370   Fluorescence Lifetime. *Langmuir* 27:7587–7594. DOI: 10.1021/la200875k.

371   Isik AT. 2010. Late onset Alzheimer's disease in older people. *Clinical Interventions in Aging*
372   5:307. DOI: 10.2147/CIA.S11718.

373   Knowles TPJ, Vendruscolo M, Dobson CM. 2014. The amyloid state and its association with
374   protein misfolding diseases. *Nature Reviews Molecular Cell Biology* 15:384–396. DOI:
375   10.1038/nrm3810.

376   Linse S. 2019. Mechanism of amyloid protein aggregation and the role of inhibitors. *Pure and*
377   *Applied Chemistry* 91:211–229. DOI: 10.1515/pac-2018-1017.

378   Ma J, Komatsu H, Kim YS, Liu L, Hochstrasser RM, Axelsen PH. 2013. Intrinsic Structural
379   Heterogeneity and Long-Term Maturation of Amyloid β Peptide Fibrils. *ACS Chemical*
380   *Neuroscience* 4:1236–1243. DOI: 10.1021/cn400092v.

381   Makin OS, Serpell LC. 2005. Structures for amyloid fibrils. *FEBS Journal* 272:5950–5961. DOI:
382   10.1111/j.1742-4658.2005.05025.x.

383   Malik R, Roy I. 2011. Probing the mechanism of insulin aggregation during agitation.
384   *International Journal of Pharmaceutics* 413:73–80. DOI: 10.1016/j.ijpharm.2011.04.024.

385 Malisauskas R, Botyriute A, Cannon JG, Smirnovas V. 2015. Flavone Derivatives as Inhibitors of
386   Insulin Amyloid-Like Fibril Formation. *PLOS ONE* 10:e0121231. DOI:
387   10.1371/journal.pone.0121231.

388 Maurer MS, Schwartz JH, Gundapaneni B, Elliott PM, Merlini G, Waddington-Cruz M, Kristen
389   A V., Grogan M, Witteles R, Damy T, Drachman BM, Shah SJ, Hanna M, Judge DP, Barsdorf
390   AI, Huber P, Patterson TA, Riley S, Schumacher J, Stewart M, Sultan MB, Rapezzi C. 2018.
391   Tafamidis Treatment for Patients with Transthyretin Amyloid Cardiomyopathy. New
392   England Journal of Medicine 379:1007–1016. DOI: 10.1056/NEJMoa1805689.

393 Mehta D, Jackson R, Paul G, Shi J, Sabbagh M. 2017. Why do trials for Alzheimer's disease drugs
394   keep failing? A discontinued drug perspective for 2010-2015. *Expert Opinion on*
395   *Investigational Drugs* 26:735–739. DOI: 10.1080/13543784.2017.1323868.

396 Meisl G, Kirkegaard JB, Arosio P, Michaels TCT, Vendruscolo M, Dobson CM, Linse S, Knowles
397   TPJ. 2016. Molecular mechanisms of protein aggregation from global fitting of kinetic
398   models. *Nature Protocols* 11:252–272. DOI: 10.1038/nprot.2016.010.

399 Milto K, Michailova K, Smirnovas V. 2014. Elongation of Mouse Prion Protein Amyloid-Like
400   Fibrils: Effect of Temperature and Denaturant Concentration. *PLoS ONE* 9:e94469. DOI:
401   10.1371/journal.pone.0094469.

402 Nettleton EJ, Tito P, Sunde M, Bouchard M, Dobson CM, Robinson C V. 2000. Characterization
403   of the Oligomeric States of Insulin in Self-Assembly and Amyloid Fibril Formation by Mass
404   Spectrometry. *Biophysical Journal* 79:1053–1065. DOI: 10.1016/S0006-3495(00)76359-4.

405 Nicoud L, Lazzari S, Balderas Barragán D, Morbidelli M. 2015. Fragmentation of Amyloid Fibrils
406   Occurs in Preferential Positions Depending on the Environmental Conditions. *The Journal of*
407   *Physical Chemistry B* 119:4644–4652. DOI: 10.1021/acs.jpcb.5b01160.

408 Nielsen L, Khurana R, Coats A, Frokjaer S, Brange J, Vyas S, Uversky VN, Fink AL. 2001. Effect
409   of environmental factors on the kinetics of insulin fibril formation: Elucidation of the
410   molecular mechanism. *Biochemistry* 40:6036–6046. DOI: 10.1021/bi002555c.

411 Park J, Egolum U, Parker S, Andrews E, Ombengi D, Ling H. 2020. Tafamidis: A First-in-Class
412   Transthyretin Stabilizer for Transthyretin Amyloid Cardiomyopathy. Annals of
413   Pharmacotherapy 54:470–477. DOI: 10.1177/1060028019888489.

414 Podestà A, Tiana G, Milani P, Manno M. 2006. Early Events in Insulin Fibrillization Studied by
415   Time-Lapse Atomic Force Microscopy. *Biophysical Journal* 90:589–597. DOI:
416   10.1529/biophysj.105.068833.

417 Ratha BN, Kar RK, Bednarikova Z, Gazova Z, Kotler SA, Raha S, De S, Maiti NC, Bhunia A.
418   2020. Molecular Details of a Salt Bridge and Its Role in Insulin Fibrillation by NMR and
419   Raman Spectroscopic Analysis. *The Journal of Physical Chemistry B* 124:1125–1136. DOI:
420   10.1021/acs.jpcb.9b10349.

421 Robbins KJ, Liu G, Selmani V, Lazo ND. 2012. Conformational analysis of thioflavin T bound to
422   the surface of amyloid fibrils. *Langmuir* 28:16490–16495. DOI: 10.1021/la303677t.

423 Sakalauskas A, Ziaunys M, Smirnovas V. 2019. Concentration-dependent polymorphism of
424   insulin amyloid fibrils. *PeerJ* 7:e8208. DOI: 10.7717/peerj.8208.

425 Selivanova OM, Galzitskaya O V. 2012. Structural polymorphism and possible pathways of
426   amyloid fibril formation on the example of insulin protein. *Biochemistry (Moscow)* 77:1237–
427   1247. DOI: 10.1134/S0006297912110028.

428 Sengupta U, Nilson AN, Kayed R. 2016. The Role of Amyloid-β Oligomers in Toxicity,
429   Propagation,   and   Immunotherapy.   *EBioMedicine*   6:42–49.   DOI:
430   10.1016/j.ebiom.2016.03.035.

431 Sidhu A, Segers-Nolten I, Raussens V, Claessens MMAE, Subramaniam V. 2017. Distinct
432   Mechanisms Determine α-Synuclein Fibril Morphology during Growth and Maturation. *ACS*
433   *Chemical Neuroscience* 8:538–547. DOI: 10.1021/acschemneuro.6b00287.

434 Sidhu A, Vaneyck J, Blum C, Segers-Nolten I, Subramaniam V. 2018. Polymorph-specific
435   distribution of binding sites determines thioflavin-T fluorescence intensity in α-synuclein
436   fibrils. *Amyloid* 25:189–196. DOI: 10.1080/13506129.2018.1517736.

437 Singh PK, Kumbhakar M, Pal H, Nath S. 2010. Viscosity Effect on the Ultrafast Bond Twisting
438   Dynamics in an Amyloid Fibril Sensor: Thioflavin-T. *The Journal of Physical Chemistry B*
439   114:5920–5927. DOI: 10.1021/jp100371s.

440 Smirnovas V, Winter R. 2008. Revealing Different Aggregation Pathways of Amyloidogenic
441   Proteins   by   Ultrasound   Velocimetry.   *Biophysical   Journal*   94:3241–3246.   DOI:
442   10.1529/biophysj.107.123133.

443 Sneideris T, Darguzis D, Botyriute A, Grigaliunas M, Winter R, Smirnovas V. 2015. pH-Driven
444   Polymorphism   of   Insulin   Amyloid-Like   Fibrils.   *PLOS   ONE*   10:e0136602.   DOI:
445   10.1371/journal.pone.0136602.

446 Sneideris T, Sakalauskas A, Sternke-Hoffmann R, Peduzzo A, Ziaunys M, Buell AK, Smirnovas
447   V. 2019. The Environment Is a Key Factor in Determining the Anti-Amyloid Efficacy of
448   EGCG. *Biomolecules* 9:1–17. DOI: 10.3390/biom9120855.

449 Sulatskaya AI, Rychkov GN, Sulatsky MI, Rodina NP, Kuznetsova IM, Turoverov KK. 2018.
450   Thioflavin T Interaction with Acetylcholinesterase: New Evidence of 1:1 Binding
451   Stoichiometry Obtained with Samples Prepared by Equilibrium Microdialysis. *ACS Chemical*
452   *Neuroscience* 9:1793–1801. DOI: 10.1021/acschemneuro.8b00111.

453 Törnquist M, Michaels TCT, Sanagavarapu K, Yang X, Meisl G, Cohen SIA, Knowles TPJ, Linse
454   S. 2018. Secondary nucleation in amyloid formation. *Chemical Communications* 54:8667–
455   8684. DOI: 10.1039/C8CC02204F.

456 Wang S-H, Dong X-Y, Sun Y. 2012. Effect of (−)-epigallocatechin-3-gallate on human insulin
457   fibrillation/aggregation kinetics. *Biochemical Engineering Journal* 63:38–49. DOI:
458   10.1016/j.bej.2012.02.002.

459 Xue C, Lin TY, Chang D, Guo Z. 2017. Thioflavin T as an amyloid dye: fibril quantification,
460   optimal concentration and effect on aggregation. *Royal Society Open Science* 4:160696. DOI:

461   10.1098/rsos.160696.

462   Zheng Q, Lazo ND. 2018. Mechanistic Studies of the Inhibition of Insulin Fibril Formation by
463   Rosmarinic Acid. *The Journal of Physical Chemistry B* 122:2323–2331. DOI:
464   10.1021/acs.jpcb.8b00689.

465   Ziaunys M, Smirnovas V. 2019a. Emergence of visible light optical properties of L-phenylalanine
466   aggregates. *PeerJ* 7:e6518. DOI: 10.7717/peerj.6518.

467   Ziaunys M, Smirnovas V. 2019b. Additional Thioflavin-T Binding Mode in Insulin Fibril Inner
468   Core Region. *The Journal of Physical Chemistry B* 123:8727–8732. DOI:
469   10.1021/acs.jpcb.9b08652.

470   Ziaunys M, Sakalauskas A, Smirnovas V. 2020. Identifying Insulin Fibril Conformational
471   Differences by Thioflavin-T Binding Characteristics. Biomacromolecules 21:4989–4997.
472   DOI: 10.1021/acs.biomac.0c01178.

473   Ziaunys M, Sneideris T, Smirnovas V. 2020. Formation of distinct prion protein amyloid fibrils
474   under identical experimental conditions. *Scientific Reports* 10:4572. DOI: 10.1038/s41598-
475   020-61663-2.

476

Figure 1

Insulin aggregation curves and their derivatives.

Normal, sigmoidal (A) and anomalous, double-sigmoidal (B) insulin aggregation kinetics and their first order derivatives (C, D respectively).
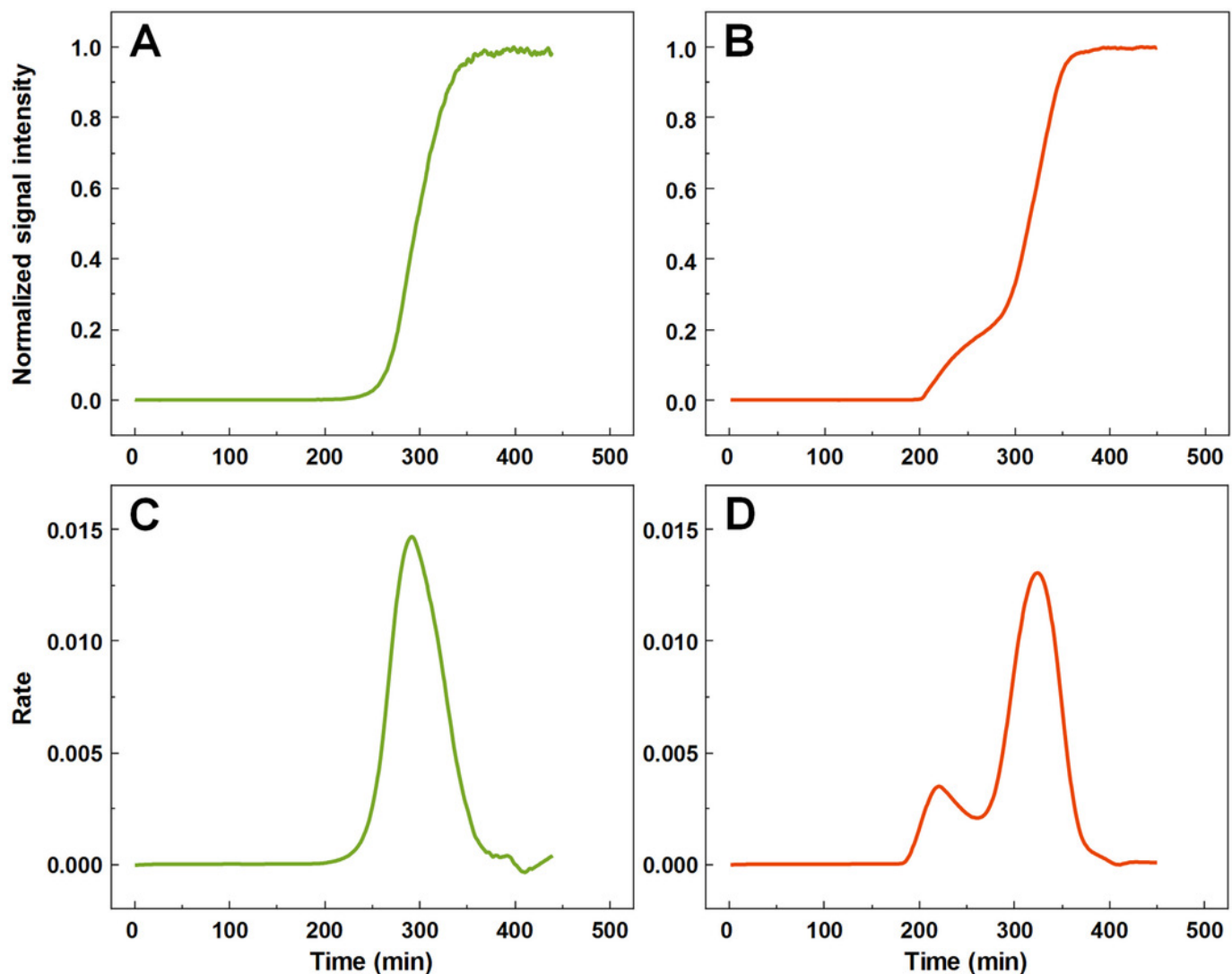
Figure 2

Distribution of maximum insulin aggregation rate, the time at which it is reached (t_r) and final fibril fluorescence intensity.

Dependence of aggregation rate on t_r (A), fluorescence intensity on t_r (B) and aggregation rate on fluorescence intensity (C). Distribution of t_r (D, G), aggregation rate (E, H) and fluorescence intensity (F, I) for normal and double-sigmoidal samples respectively. Color-coded numbers, displayed above peak-fit curves, indicate peak maximum values.
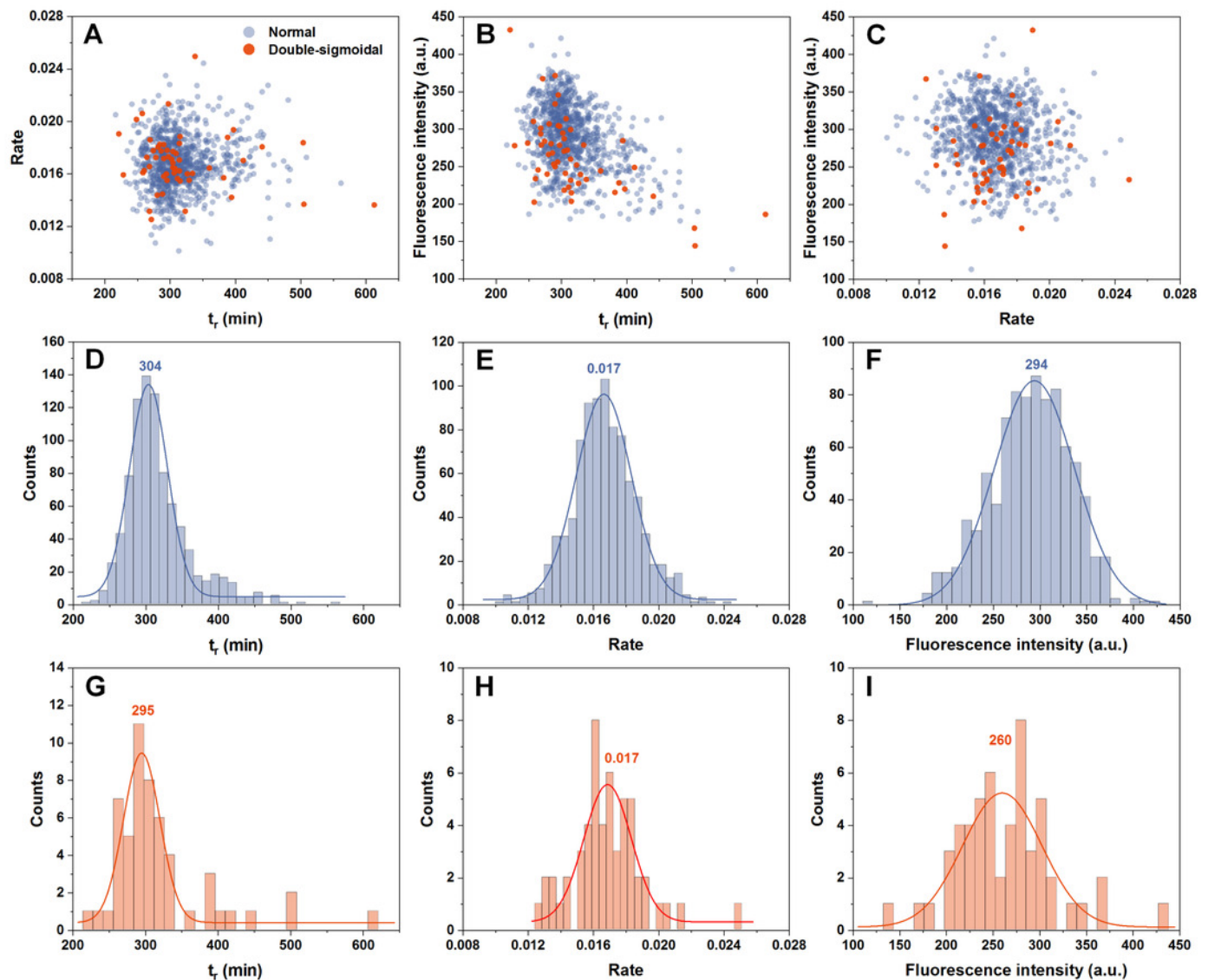
Figure 3

Normal, intermediate and double-sigmoidal sample AFM images, fibril height distributions, second order FTIR spectra and seeding kinetics.

AFM images of insulin aggregates during the first part of the double-sigmoidal kinetics (A) and at the end of normal (B) and double-sigmoidal (C) aggregation. Height distribution of double-sigmoidal aggregation intermediates and fibrils after normal and double-sigmoidal aggregation (D), where box plots indicate the interquartile range and error bars are one standard deviation. Second order FTIR spectra (E) and seeded aggregation kinetics (F).
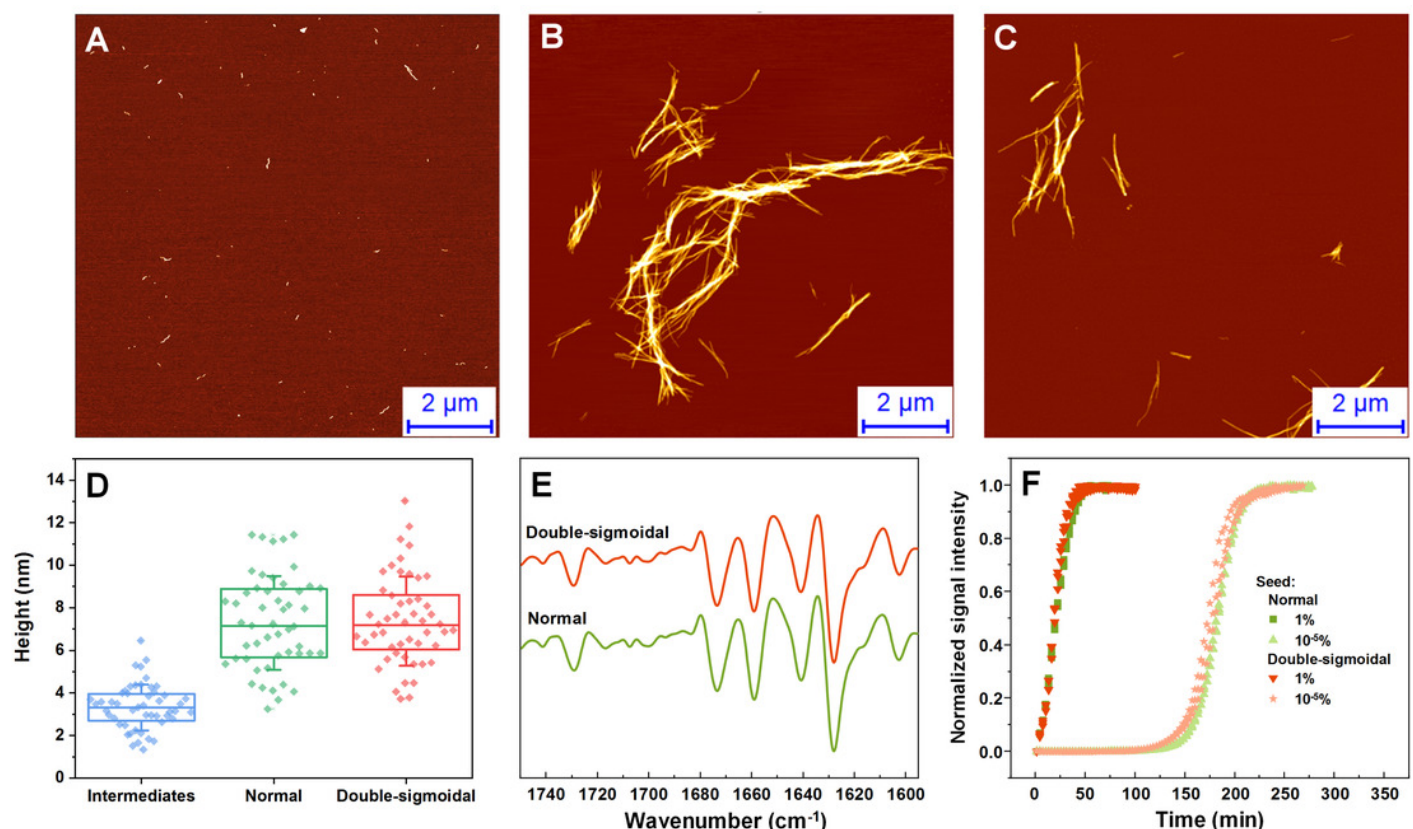
Figure 4

Insulin aggregation kinetics and bound ThT fluorescence EEMs.

Insulin aggregation kinetics monitored by scanning ThT fluorescence EEMs (A), where each data point is the maximum value in the recorded EEM. EEM "center of mass" excitation (B) and emission (C) wavelengths over the course of aggregation. Top intensity values present in the ThT EEMs at different aggregation time points (D) during the first double-sigmoidal increase (darker green areas represent higher intensity zones). The red * symbol indicates the point where there is a sudden jump in ThT fluorescence intensity. Data in part (A) was fit using a Boltzmann's sigmoidal equation with the anomalous aggregation phase data points omitted from the fitting procedure.